OLD DOMINION UNIVERSITY RESEARCH FOUNDATION

DEPARTMENT OF MECHANICAL ENGINEERING AND MECHANICS
SCHOOL OF ENGINEERING
OLD DOMINION UNIVERSITY
NORFOLK, VIRGINIA

LAMINAR AND TURBULENT FLOW SOLUTIONS WITH RADIATION AND ABLATION INJECTION FOR JOVIAN ENTRY

By

Ajay Kumar
and
S. N. Tiwari, Principal Investigator

Final Report
For the period ending February 29, 1980

Prepared for the
National Aeronautics and Space Administration
Langley Research Center
Hampton, Virginia

Under
Research Grant NSG 1464
Randolph A. Graves, Jr. and Jim J. Jones, Technical Monitors
Space Systems Division

May 1980

DEPARTMENT OF MECHANICAL ENGINEERING AND MECHANICS
SCHOOL OF ENGINEERING
OLD DOMINION UNIVERSITY
NORFOLK, VIRGINIA

LAMINAR AND TURBULENT FLOW SOLUTIONS WITH RADIATION AND ABLATION INJECTION FOR JOVIAN ENTRY

By

Ajay Kumar
and
S. N. Tiwari, Principal Investigator

Final Report
For the period ending February 29, 1980

Prepared for the
National Aeronautics and Space Administration
Langley Research Center
Hampton, Virginia 23665

Under
Research Grant NSG 1464
Randolph A. Graves, Jr. and Jim J. Jones, Technical Monitors
Space Systems Division

Submitted by the
Old Dominion University Research Foundation
P. O. Box 6369
Norfolk, Virginia 23508

May 1980

FOREWORD

This report covers the final work completed on the research project "Effects of Angle of Attack on the Coupled Radiative and Convective Heat Transfer About Blunt Planetary Entry Bodies." The work was supported by the NASA/Langley Research Center (Aerothermodynamics Branch of the Space Systems Division) through research grant NSG-1464. The grant was initially monitored by Dr. Randolph A. Graves, Jr. of the Space Systems Division. In recent months, the grant has been monitored by Mr. Jim J. Jones of the Space System Division.

TABLE OF CONTENTS

LIST OF TABLES

LIST OF FIGURES

(Continued)

LIST OF FIGURES (CONCLUDED)

LAMINAR AND TURBULENT FLOW SOLUTIONS WITH RADIATION AND ABLATION INJECTION FOR JOVIAN ENTRY

By

Ajay Kumar[1] and S. N. Tiwari[2]

SUMMARY

Laminar and turbulent flow-field solutions with coupled carbon-phenolic mass injection are presented for the forebody of a probe entering a nominal Jupiter atmosphere. Solutions are obtained for a 35-degree hyperboloid and for a 45-degree spherically blunted cone using a time-dependent, finite-difference method. The radiative heating rates for the coupled laminar flow are significantly reduced as compared to the corresponding no-blowing case; however, for the coupled turbulent flow, it is found that the surface radiative heating rates are substantially increased and often exceed the corresponding no-blowing values. Turbulence is found to have no effect on the surface radiative heating rates for the no-blowing solutions. The present results are compared with the other available solutions, and some additional solutions are presented.

INTRODUCTION

The entry probe for the NASA Galileo mission to the planet Jupiter will encounter very severe aerodynamic heating due to exceedingly high entry velocities. A massive heat shield will be required on the probe's surface to protect the scientific instruments from this aerodynamic heating. To reduce the uncertainties in the design of the heat shield, it is necessary to accurately predict the entry aerothermal environment. Since it is

---

[1] Research Associate Professor, Department of Mechanical Engineering and Mechanics, Old Dominion University, Norfolk, Virginia 23508.

[2] Eminent Professor, Department of Mechanical Engineering and Mechanics, Old Dominion University, Norfolk, Virginia 23508.

extremely difficult to duplicate the entry environment in an experimental facility, the design of the heat shield for the Galileo probe relies primarily on analytical predictions.

In order to predict the flow-field accurately, one must model all the physical phenomena occurring in the flow. For the Galileo proble, the gases surrounding the probe forebody will have temperatures in the range of 10,000 to 20,000 K, and the surface heating will be primarily due to radiative heating. This will result in massive ablation of the probe's heat shield. Moreover, the flow is expected to be mostly turbulent. The analytical technique should include all the above-mentioned phenomena in order to accurately predict the surface heating rates and other flow characteristics.

Reference 1 presented laminar and turbulent flow-field solutions for the analytic-shaped bodies (hyperboloids) using a nominal entry trajectory for Jupiter. The viscous shock-layer analysis included coupled ablation injection, detailed spectral calculation of radiative heating, and equilibrium chemistry. In reference 2, this analysis was further used to obtain some coupled turbulent flow-field solutions for the forebody of a 45-degree spherically blunted cone (Galileo-probe configuration) only at certain times of the nominal entry trajectory. No solutions could be obtained for the laminar coupled flow field. Reference 3 has presented coupled turbulent solutions for the Galileo probe using an approximate method which assumes a shock shape and then predicts the body shape. There still is a great need for an analytical technique which can accurately predict the coupled laminar and turbulent flow fields for the trajectory. The purpose of the present study was to develop such a technique.

In reference 4, a time-asymptotic, finite-difference method was developed to predict the forebody flow field past blunt axisymmetric bodies, such as spherically blunted cones, hyperboloids, etc., at zero and small angles of attack. The method uses time-dependent, viscous, shock-layer equations to describe the flow field. The analysis was modified in reference 5 for the laminar and turbulent flow of a radiating and reacting gas under chemical equilibrium. It was found in reference 6 that the method works well for both the laminar and turbulent flows even in the presence of massive surface blowing.

The present investigation uses the above method for obtaining the laminar and turbulent flow-field solutions for a 35-degree hyperboloid and a 45-degree spherically blunted cone (Galilec probe shape). The analysis includes coupled ablation injection, detailed spectral calculation of radiative heating, and equilibrium chemistry. The radiative heat transfer and equilibrium chemistry calculations are made using the same techniques used in reference 1. The results of the present analysis are compared with those of references 2 and 3, and additional solutions are presented for the conditions for which reference 2 presents no solution.

LIST OF SYMBOLS

C_A ablator mass fraction

C_i mass fraction of species i, ρ_i/ρ

C_ℓ mass fraction of element ℓ

H total enthalpy, $\overline{H}/\overline{V}_\infty^2$

h enthalpy of mixture, $\sum_{i=1}^{N} C_i h_i$

$\overline{h}_A$ enthalpy of undecomposed ablation material

h_i enthalpy of species i, $\overline{h}_i/\overline{V}_\infty^2$

k thermal conductivity of mixture, $\overline{k}/\left(\overline{\mu}_\infty \overline{V}_\infty^2/\overline{T}_\infty\right)$

Le Lewis number

Le_T turbulent Lewis number

$\overline{M}_\ell$ molecular weight of mixture

$\overline{M}_i$ molecular weight of species i

$\overline{M}_\ell$ molecular weight of element ℓ

$\dot{m}$ mass injection rate, $\overline{\dot{m}}/\overline{\rho}_\infty \overline{V}_\infty$

N number of species

n coordinate normal to the body, $\overline{n}/\overline{R}_n$

N_H number density of atomic hydrogen (particles/cm^3)

p pressure, $\overline{p}/\overline{\rho}_\infty \overline{V}_\infty^2$

q^R	net radiative heat flux in n-direction, $\bar{q}^R/\bar{\rho}_\infty \bar{V}_\infty^3$
q^{R+}	component of radiative flux towards the shock
q^{R-}	component of radiative flux towards the wall
$-q_w^C$	convective heat flux to the wall
R^*	universal gas constant (J/mole°K)
$\bar{R}_n$	nose radius (m)
Re	free-stream Reynolds number, $\bar{\rho}_\infty \bar{V}_\infty \bar{R}_n/\bar{\mu}_\infty$
r	radium measured from axis of symmetry to point on body surface, $\bar{r}/\bar{R}_n$
s	coordinate measured along the body, $\bar{s}/\bar{R}_n$
Sc	Schmidt number
T	temperature, $\bar{T}/\bar{T}_\infty$
$\bar{T}_\infty$	free-stream temperature (°K)
t	nondimensional time, $\bar{t}\bar{V}_\infty/\bar{R}_n$
u	tangential velocity, $\bar{u}/\bar{V}_\infty$
u_s	tangential velocity at shock, $\bar{u}_s/\bar{V}_\infty$
v	normal velocity, $\bar{v}/\bar{V}_\infty$
V_∞	free-stream velocity (m/sec)
β	$r + n \cos\theta$
$\beta_{i,j}$	coefficients for sublimation temperature [eq. (5)]
δ_s	shock standoff distance, $\bar{\delta}_s/\bar{R}_n$
$\delta_{i\ell}$	number of atoms of the ℓth element in species i
ε_+	emissivity
ε	normalized eddy viscosity, μ_T/μ
θ	body angle measured from the body axis
κ	local body curvature, $\bar{\kappa}\bar{R}_n$
λ	$1 + n\kappa$

μ viscosity, $\bar{\mu}/\bar{\mu}_\infty$

μ_T eddy viscosity, $\bar{\mu}_T/\bar{\mu}_\infty$

$\bar{\mu}_\infty$ free-stream viscosity (N sec/m^2)

ρ density, $\bar{\rho}/\bar{\rho}_\infty$

$\bar{\rho}_\infty$ free-stream density (kg/m^3)

σ Prandtl number

σ_T turbulent Prandtl number

$\bar{\sigma}$ Stefan Boltzmann constant

Superscript

$(\bar{\ })$ dimensional quantities

Subscript

i ith species

ℓ ℓth element

s shock values

sub sublimation

w wall values

∞ free-stream values

$-$ values for the solid ablation material at the surface

o stagnation point

ANALYSIS

Governing Equations

The equations of motion for the laminar and turbulent flows of reacting gas mixtures in chemical equilibrium are given in reference 5. These viscous shock-layer-type equations are modified for the present analysis to include

the elemental continuity equation which is required here due to the surface ablation injection. The governing equations in the body-oriented coordinate system (fig. 1) for the flow at zero angle of attack are expressed as

$$\frac{\partial U}{\partial t} + \frac{\partial M}{\partial s} + \frac{\partial \hat{N}}{\partial n} + Q = 0 \tag{1}$$

where

$$U = \lambda \begin{bmatrix} \rho \\ \rho u \\ \rho v \\ \rho H - p \\ \rho C_{\ell} \end{bmatrix}, \qquad M = \begin{bmatrix} \rho u \\ p + \rho u^2 \\ \rho uv \\ \rho uH \\ \rho uC_{\ell} \end{bmatrix}$$

$$\hat{N} = \lambda \begin{bmatrix} \rho v \\ \rho uv - \tau \\ p + \rho v^2 \\ \left\{ \rho vH - \frac{\mu}{\sigma Re} \left(1 + \epsilon^{+} \frac{\sigma}{\sigma_T}\right) \frac{\partial h}{\partial n} - \mu\tau \right. \\ \left. - \frac{\mu}{\sigma Re} \left[Le - 1 + \epsilon^{+} \frac{\sigma}{\sigma_T} \left(Le_T - 1 \right) \right] \sum_{i=1}^{N} h_i \frac{\partial C_i}{\partial n} + qR \right\} \\ \rho vC_{\ell} - \frac{\mu}{\sigma Re} \left(Le + \epsilon^{+} \frac{\sigma}{\sigma_T} Le_T \right) \frac{\partial C_{\ell}}{\partial n} \end{bmatrix}$$

$$Q = \frac{\lambda \sin\theta}{\beta} M + \frac{\cos\theta}{\beta} \hat{N} +$$

$$\frac{1}{\beta} \begin{bmatrix} 0 \\ \beta\kappa(\rho uv - \tau) - p\lambda \sin\theta \\ -\beta\kappa\rho u^2 - p(\lambda \cos\theta + \beta\kappa) \\ 0 \\ 0 \end{bmatrix}$$

Here

$$C_\ell = \sum_{i=1}^{N} \delta_{\ell i} \frac{\bar{M}_\ell}{\bar{M}_i} C_i$$

and

$$\tau = \mu(1 + \varepsilon^+)/Re(\partial u/\partial n - u\kappa/\lambda).$$

The above equations are not valid at the axis of symmetry where $\beta = 0$. A limiting form of the governing equations is obtained at $s = 0$ by differentiating equation (1) with respect to s and taking a limit as $s \to 0$. The following equations are obtained at the axis of symmetry:

$$\frac{\partial U_o}{\partial t} + \frac{\partial M_o}{\partial s} + \frac{\partial \hat{N}_o}{\partial n} + Q_o = 0 \qquad (2)$$

where

$$U_o = \lambda \begin{bmatrix} \rho \\ \rho u \\ \rho V \\ \rho H - p \\ \rho C_\ell \end{bmatrix}, \quad M_o = \begin{bmatrix} 2\rho u \\ p + 2\rho u^2 \\ 2\rho uv \\ 2\rho uH \\ 2\rho u C_\ell \end{bmatrix}$$

$$\hat{N}_o = \lambda \begin{bmatrix} \rho v \\ \rho uv - \tau \\ p + \rho v^2 \\ \left\{ \rho vH - \frac{\mu}{\sigma Re} \left(1 + \epsilon^+ \frac{\sigma}{\sigma_T}\right) \frac{\partial h}{\partial n} - u\tau - \frac{\mu}{\sigma Re} \left[Le - 1 + \epsilon^+ \frac{\sigma}{\sigma_T} \right. \right. \\ \left. \left. \cdot \left(Le_T - 1\right)\right] \sum_{i=1}^{N} h_i \frac{\partial C_i}{\partial n} + q^R \right\} \\ \rho v C_\ell - \frac{\mu}{\sigma Re} \left(Le + \epsilon^+ \frac{\sigma}{\sigma_T} Le_T\right) \frac{\partial C_\ell}{\partial n} \end{bmatrix}$$

$$Q_o = \kappa \begin{bmatrix} \rho v \\ 2(\rho uv - \tau) \\ \left[-p + \rho(v^2 - u^2)\right] \\ \left\{ \rho vH - \frac{\mu}{\sigma Re} \left(1 + \epsilon^+ \frac{\sigma}{\sigma_T}\right) \frac{\partial h}{\partial n} - u\tau - \frac{\mu}{\sigma R_e} \right. \\ \left. \left[Le - 1 + \epsilon^+ \frac{\sigma}{\sigma_T} \left(Le_T - 1\right)\right] \sum_{i=1}^{N} h_i \frac{\partial C_i}{\partial n} + q^R \right\} \\ \rho v C_\ell - \frac{\mu}{\sigma Re} \left[Le + \epsilon^+ \frac{\sigma}{\sigma_T} Le_T\right] \frac{\partial C_\ell}{\partial n} \end{bmatrix}$$

The equation of state is given by

$$p = \left(\frac{R^* \bar{T}_\infty}{\bar{M}\, \bar{V}_\infty^2}\right)\rho T \tag{3}$$

Two independent variable transformations are applied to the governing equations. The first transformation maps the computational domain into a rectangular region in which both the shock and the body are made boundary mesh lines. The second transformation further maps the computational region into another plane to allow higher resolution near the body surface without any significant increase in the number of mesh points in the normal direction. The details of these transformations are given in reference 4.

Boundary Conditions

No-slip boundary conditions are used at the surface. The wall temperature and mass injection rate are either specified or calculated. The boundary conditions at the shock are calculated by using the shock relations.

For the calculated mass injection conditions, the ablation process is assumed to be quasi-steady and the wall temperature is the sublimation temperature of the ablator surface. The coupled mass injection rate is then given by

$$\dot{m} = \left(\frac{-\bar{q}_w^C - \bar{q}_w^R}{\sum_{i=1}^{N} \left(C_i \bar{h}_i\right)_w - \bar{h}_A}\right) / \bar{\rho}_\infty \bar{V}_\infty \tag{4}$$

The sublimation temperature for the carbon-phenolic ablator is given by

$$\bar{T}_{sub} = \sum_{j=1}^{5} \beta_{1,j} C_A^{j-1} + \log \bar{p}_w \sum_{j=1}^{5} \beta_{2,j} C_A^{j-1}$$

$$+ \left(\log \bar{p}_w\right)^2 \sum_{j=1}^{5} \beta_{3,j} C_A^{j-1} \tag{5}$$

where $\bar{p}_w$ is the wall pressure in atmospheres and C_A is the ablator mass fraction at the wall. The values of $\beta_{i,j}$ are given in table 1. These are applicable for a free-stream gas composition of 89 percent H_2, 11 percent He by volume, and for ablator mass fractions of 0.4 to 1.0.

For ablation injection, the elemental concentrations at the wall are governed by convection and diffusion as given by the equation

$$\left(\frac{\partial C_\ell}{\partial n}\right)_w - \frac{1}{Re}\left(\frac{\dot{m}\,Sc}{\mu}\right)_w \left[(C_\ell)_w - (C_\ell)_-\right] = 0 \tag{6}$$

The net radiative flux, q^R, can be represented as

$$q^R = q^{R^+} - q^{R^-} \tag{7}$$

At the surface

$$\bar{q}_w^{R^+} = \varepsilon\ \bar{\sigma}\ \bar{T}_w^4 \tag{8}$$

The surface is treated as a gray surface with an assumed emissivity ε of 0.8 and a reflectivity of 0.0. The heat transferred to the wall due to conduction and diffusion is

$$-q_w^C = \frac{1}{Re}\left(k\frac{\partial T}{\partial n} + \frac{\mu}{Sc}\sum_{i=1}^{N} h_i \frac{\partial C_i}{\partial n}\right)_w \tag{9}$$

Radiative Transport

The radiative flux, q^R, is calculated with the radiative transport code RAD (refs. 7,8) which has been incorporated into the present computer code.

The RAD accounts for the effects of nongray self absorption. Molecular band, continuum, and atomic line transitions are included. A detailed frequency dependence of the absorption coefficients is used for integrating over the radiation frequency spectrum, and the tangent slab approximation is used for integrating over physical space. The chemical species considered in the present study for determining the radiative transport are H, H_2, H^+, e^-, C, C_2,

C_3, C^+, C^-, CO, O, O_2, O^+, and O^-. The radiation properties used in this study for C_2 and C_3 are those reported in references 9 and 10, respectively.

Thermodynamic and Transport Properties

The equilibrium composition is determined by a free energy minimization calculation as developed in reference 11 and written for the present code in reference 12. Thermodynamic properties for specific heat, enthalpy, and free energy and transport properties for viscosity and thermal conductivity are required for each species considered. Values for the thermodynamic and transport properties are obtained by using polynomial curve fits. Mixture viscosity is obtained by using the semi-empirical formula of Wilke (ref. 13).

Six chemical species are used to describe the hydrogen-helium gas mixture: e^-, H, H_2, H^+, He, and He^+. With carbon-phenolic injection, 13 additional species are used: C, C_2, C_3, C^+, C_2H, C_3H, C_4H, C_2H_2, O, O_2, O^+, CO, and CO_2. The Lewis number and Prandtl number of the mixture are set equal to 1.1 and 0.64, respectively.

Eddy-Viscosity Approximations

A two-layer, eddy-viscosity model consisting of an inner law based upon Prandtl's mixing-length concept and the Clauser-Klebanoff expression (based on refs. 14 and 15) for the outer law is used in the present investigation. This model, introduced by Cebeci (ref. 16), assumes that the inner law is applicable for the flow from the wall out to the location where the eddy viscosity given by the inner law is equal to that of the outer law. The outer law is then assumed applicable for the remainder of the viscous layer. It is noted that the eddy viscosity degenerates to approximately zero in the inviscid portion of the shock layer. The degeneracy is expressed in terms of the normal intermittency factor given by Klebanoff (ref. 15). Reference 2 gives a more detailed description of the turbulence model and various expressions for it. The only difference between the models used in the present calculations and that used in reference 2 is in the boundary-layer edge definition. The present analysis uses the definition given in reference 17, which is based on an index of diffusion, conduction, and dissipation. The turbulent Prandtl number and Lewis number are assumed to be 0.9 and 1.0, respectively.

METHOD OF SOLUTION

A time-asymptotic, two-step, finite-difference method due to MacCormack (ref. 18) is used to solve the governing equations. The details of the method are given in reference 4.

The calculations of equilibrium chemistry, radiative heat flux, and eddy viscosity require a significant amount of computing time, and it is not feasible to perform these calculations in each time-step. In the present analysis, the eddy viscosity is calculated after every 25 time-steps, the equilibrium chemistry after every 200 time-steps, and the radiative heat flux after every 1,000 or 2,000 time-steps.

RESULTS AND DISCUSSION

Forebody flow-field solutions and surface heating rates are presented for a probe entering a nominal Jupiter atmosphere. Most of the results are obtained for the flow past a 45-degree sphere-cone (the current Galileo probe configuration), but a sample calculation is made for the flow past a 35-degree (asymptotic half angle) hyperboloid for comparison with the existing results. The free-stream conditions correspond to an entry trajectory into the Jupiter atmosphere where the atmospheric gas model is the Orton nominal atmosphere consisting of 89 percent of H_2 and 11 percent He by volume (see ref. 2 for further details). These free-stream conditions are tabulated in table 2. The nose radius of the probe is 0.3112 m.

In this study, solutions are obtained for both laminar and turbulent flows with and without coupled ablation injection. In all the turbulent solutions, transition from laminar to turbulent flow is assumed to occur instantaneously at the first mesh point away from the stagnation point, which is at $s = 0.157$. Both laminar and turbulent solutions are compared with the existing results for the hyperboloid, but only turbulent solutions are available for the sphere cone.

Figures 2 and 3 show the surface heating rates with and without coupled ablation injection for the sphere-cone at 111.3 sec. It is seen from figure 2 that the turbulence has no effect on the radiative heating rates for no-injection,

but the turbulent convective heating rates are much higher than the laminar convective heating rates, as is seen from figure 3. The radiative heating rates for the coupled laminar flow are significantly reduced all over the body and the convective heating rates are negligible. However, the radiative heating rates for the coupled turbulent flow are seen to increase again as compared to the coupled laminar flow and, in fact, are even higher than the no-injection radiative heating rates on the conical portion of the probe. This adverse effect of turbulence on the radiative heating rates was first reported in reference 2. The coupled turbulent convective heating rates also increase but still are only a small fraction of the corresponding radiative heating rates. Thus, it is concluded from figure 2 that the coupled turbulent radiative heating rates are critical for the design of the probe's heat shield. The enhancement of the radiative heating rates due to turbulence will be discussed later.

Figure 4 shows a comparison of coupled radiative heating rates for the laminar and turbulent flows over the 35-degree hyperboloid with reference 2. It is seen that the present laminar radiative heating rates are about 5 to 10 percent higher and the present turbulent radiative heating rates are about 20 percent higher than those predicted in reference 2. This difference is partially due to the fact that, in reference 2, the mass injection rate at a particular body station is calculated by using the heating rate at the previous body station. Since the heating rates over the body are seen to decrease with increasing body distance, the mass injection rate at a particular body station used in reference 2 is higher than it should be if the heating rate at that same body station is used. This higher mass injection rate results in a slight decrease in the radiative heating rate. Ths present analysis uses the heating rate at the same body station at which the mass injection rate is being calculated. Another difference between the present results and those of reference 2 is that the present analysis does not predict any overshoot in the turbulent radiative heating rates near the stagnation region.

Figure 5 shows the comparison of the corresponding surface mass injection rates. It is seen that although the present laminar radiative heating rates are slightly higher than those in reference 2, the present surface mass injection rates are still lower. This is directly due to the reason given earlier. The present turbulent mass injection rates are higher on the downstream part of

the body, but the difference is not as much as it was between the radiative heating rates. This decrease in the difference in the mass injection rates is also due to the reason discussed earlier.

Shock standoff distances are compared in figure 6. The present analysis predicts about 10 percent high... shock standoff distances for the turbulent flow, but the shock standoff distances for the laminar flow compare well. All the results presented below are for the flow past a sphere cone.

Figures 7 and 8 show the coupled laminar and turbulent radiative heating rates and surface mass injection rates at 111.3 sec. The results of reference 2 are also plotted for comparison. It is seen that the present results are about 10 to 15 percent higher on the conical portion of the probe. Unlike reference 2, the present heating rates and mass injection rates gradually decrease on the nose portion of the probe. No comparison could be made for the coupled laminar flow as the method of reference 2 does not work for the coupled laminar flow past a sphere cone.

Figure 9 shows the surface pressure distribution for the coupled laminar and turbulent flows at 111.3 sec along with the surface pressure distribution predicted in reference 2 for the coupled turbulent flow. It is seen from the present results that the surface blowing smoothes out the effect of curvature discontinuity at the juncture point of the probe. The surface pressures for the turbulent flow as predicted by the two analyses compare well in the nose region and on the conical portion of the probe, but the results of reference 2 show a sharp decrease and then increase in the pressure around the juncture point. This behavior of the surface pressure in the presence of massive surface blowing is not physically expected.

Figures 10 and 11 show the coupled laminar and turbulent radiative heating rates at 109 and 107.2 seconds. The method of reference 2 fails to work for these trajectory points, but coupled turbulent radiative heating rates are given in reference 3. The present radiative heating rates are about 25 percent higher than those predicted in references 3. Figure 12 shows the corresponding mass injection rates. The nondimensional mass injection rate $\dot{m}$ is maximum for 107.2 sec out of the three trajectory points considered in the present analysis. For other trajectory points, $\dot{m}$ is also

expected to be lower than for 107.2 sec. Since the present method worked well for 107.2 sec, it should be able to provide solutions at any point on the trajectory given in table 2.

Figures 13 through 16 show the effect of turbulence on the shock layer. It is seen from these figures that the turbulence significantly changes the structure of the shock layer. The profiles of reference 2 for the turbulent flow are also plotted for comparison. In general, the present flow profiles show distributions similar to those in reference 2. Tangential velocity and temperature profiles are shown in figures 13 and 14. These profiles show the same behavior as observed in reference 6 in the presence of massive surface blowing. The gradients near the surface significantly increase for the turbulent flow and the turbulence brings the high-temperature gases closer to the surface. Figure 15 shows that, for the turbulent flow, the ablation layer (the portion of the shock layer in which the ablation products are dominantly present) is much thicker, but the concentration of the ablation products is decreased due to enhanced diffusion. Figure 16 shows the number density distributions of C_2 and C_3 for laminar and turbulent flows. It is seen that the number densities of C_2 and C_3 for the turbulent flow are significantly reduced as compared to the corresponding laminar values. The high temperatures near the surface for the turbulent flow dissociate these molecules, thus reducing their concentrations. It is shown in reference 10 that C_2 and C_3 are the main radiation-absorbing molecules for Jovian entry conditions. Thus, the turbulence has an adverse effect on the effectiveness of the ablation species to absorb radiation.

CONCLUSIONS

A time-dependent, finite-difference method is used to develop a code for solving the coupled laminar and turbulent flows over the forebody of a probe entering a nominal Jupiter atmosphere. Solutions are obtained for both a 35-degree hyperboloid and a 45-degree sphere cone. Detailed comparisons are made with the existing results. It is found that the present code works well for both the coupled laminar and turbulent flows at all the trajectory points. The code used in reference 2 works well for both the coupled laminar and turbulent flows over a hyperboloid, but it works only for the coupled turbulent

flows over a sphere cone. Even for the coupled turbulent flows, it does not work at several trajectory points where the nondimensional injection rates are very high, such as at 109 or 107.2 sec. The present code uses the heating rate at the same point for which the injection rate is being calculated, whereas in reference 2 the heating rate at the previous mesh point is used.

The turbulence is found to alter the structure of the shock layer in such a way that the effectiveness of the ablation layer is significantly reduced. The present analysis supports the finding of reference 2, in which the coupled radiative heating rates exceed even the no-injection values on the conical portion of the body. The present coupled, turbulent, radiative heating rates have the maximum value at the stagnation point, whereas the results of references 2 and 3 show the maximum to be slightly downstream of the stagnation point. The surface pressures predicted by the present analysis appear to be more physically plausible in the presence of massive surface blowing than those in reference 2, where a very sharp dip occurs around the sphere-cone juncture point. Detailed flow-field profiles are similar to those in reference 2, but there are differences in the magnitude.

Table 1. Sublimation temperature coefficients.

Coefficients	j				
	1	2	3	4	5
$\beta_{1,j}$	5552	-20184	53058	-57933	23243
$\beta_{2,j}$	1798	-12049	30145	-32045	12457
$\beta_{3,j}$	322	- 2208	5270	- 5450	2092

Table 2. Free-stream conditions.

Time from entry point (sec)	Altitude (km)	$\bar{V}_\infty$ (km/sec)	$\bar{\rho}_\infty$ (kg/m^3)
99.9	195.56	48.07	$2.65*10^{-5}$
103.9	169.57	46.96	$7.19*10^{-5}$
107.2	149.10	44.83	$1.64*10^{-4}$
109.0	138.60	42.88	$2.54*10^{-4}$
110.2	131.90	41.16	$3.38*10^{-4}$
111.3	126.05	39.29	$4.36*10^{-4}$
112.2	121.49	37.52	$5.34*10^{-4}$
113.5	115.31	34.67	$7.02*10^{-4}$
114.2	112.20	33.01	$8.05*10^{-4}$
115.3	107.63	30.31	$9.89*10^{-4}$
116.4	103.45	27.54	$1.20*10^{-3}$
117.4	100.00	25.07	$1.41*10^{-3}$

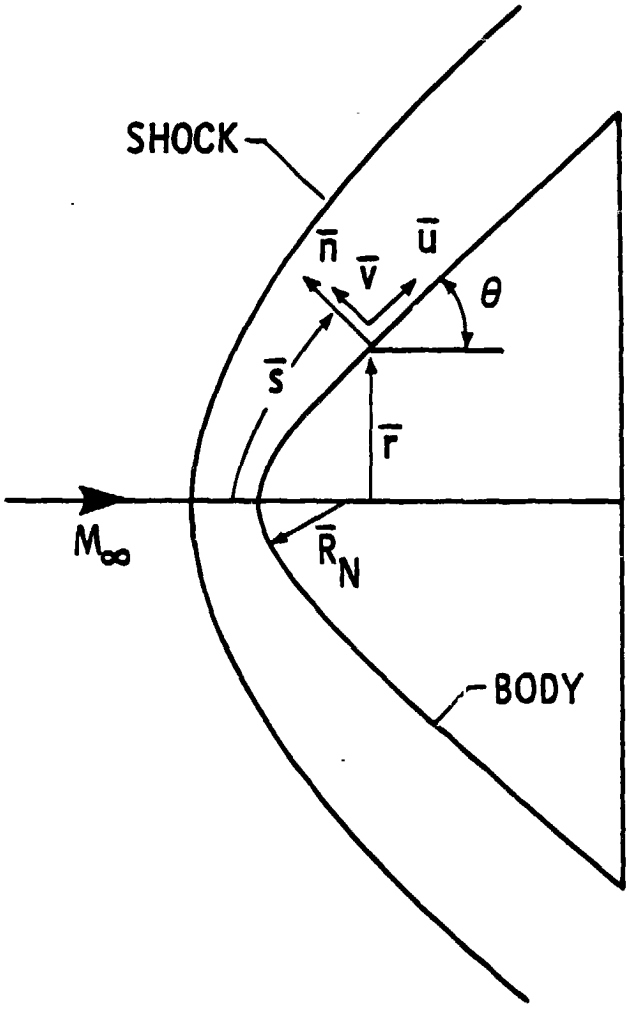

Figure 1. Coordinate system.

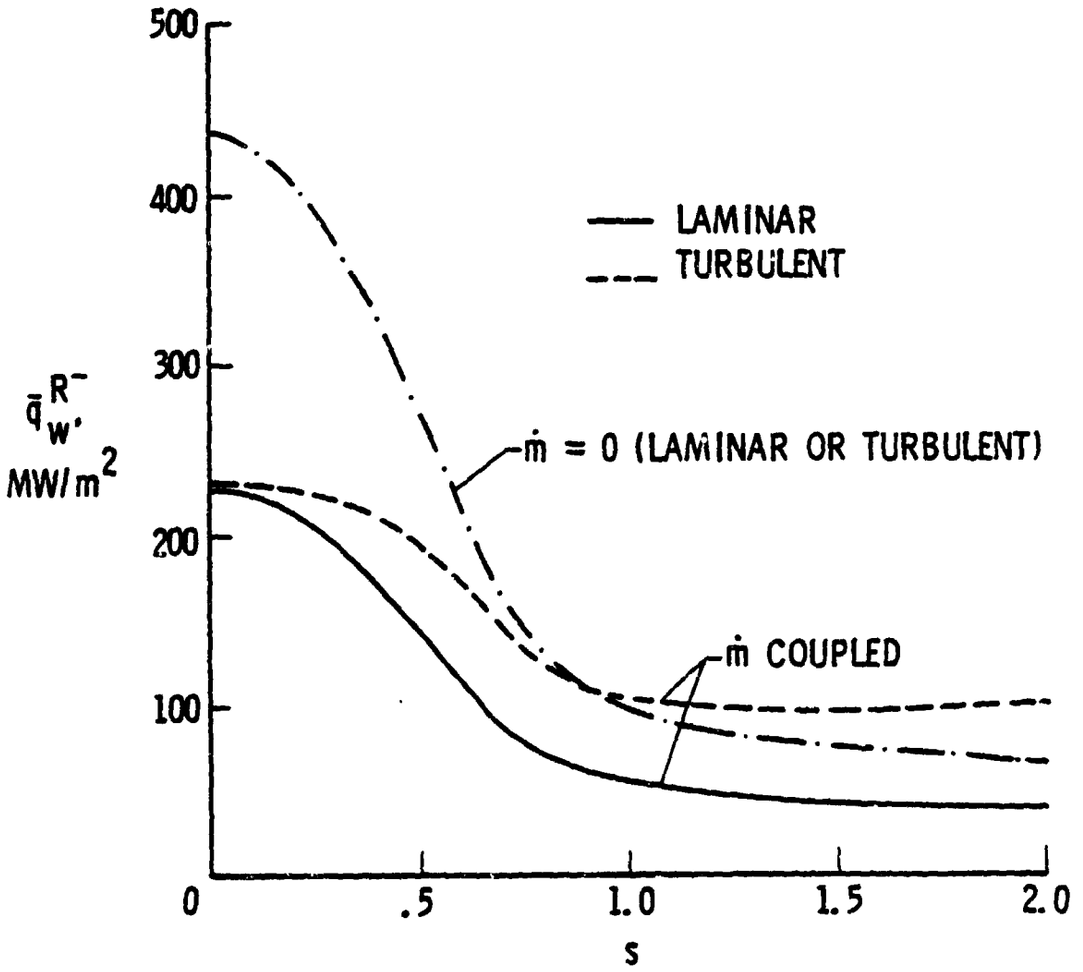

Figure 2. Effect of coupled carbon-phenolic injection on radiative heating rates for a 45-degree sphere cone at 111.3 sec.

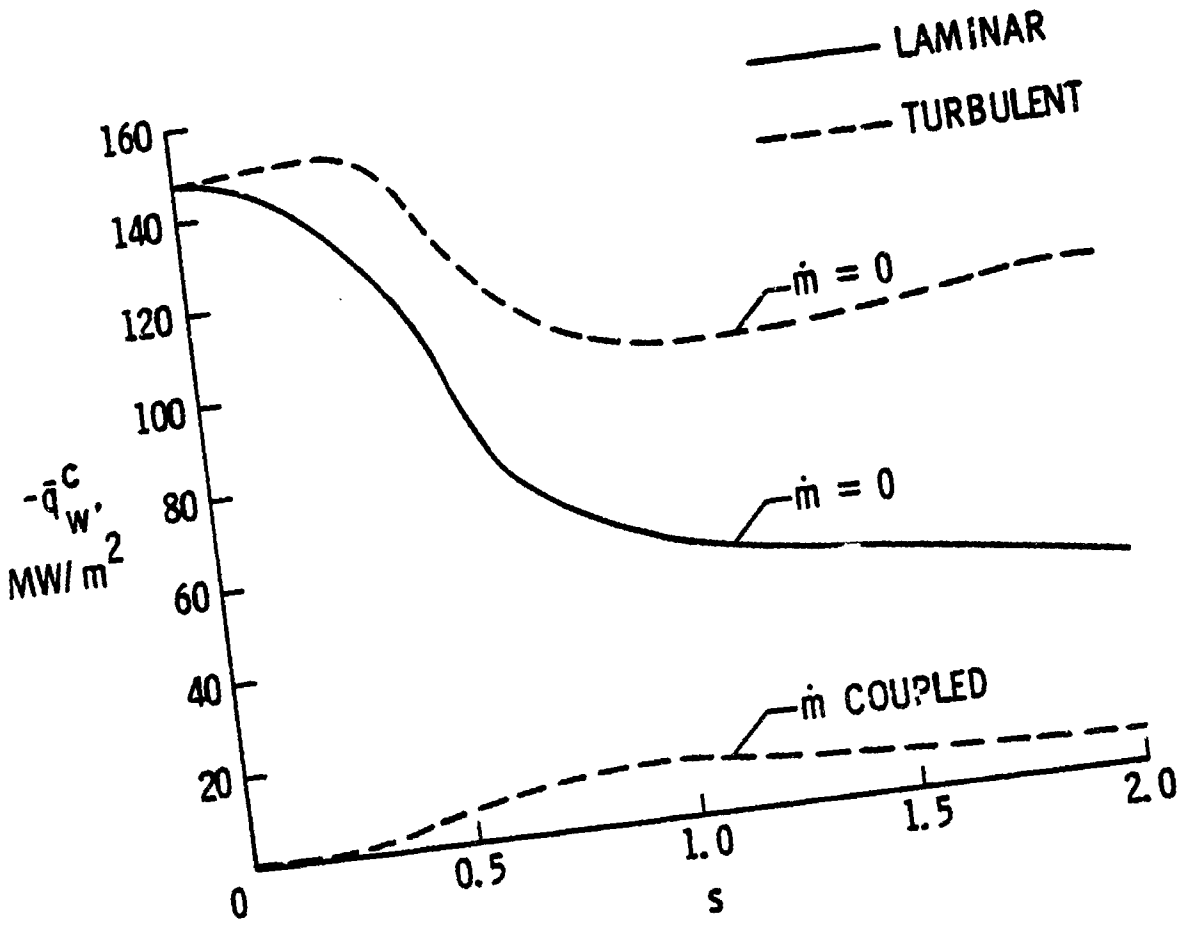

Figure 3. Effect of coupled carbon-phenolic injection on convective heating rates for a 45-degree sphere cone at 111.3 sec.

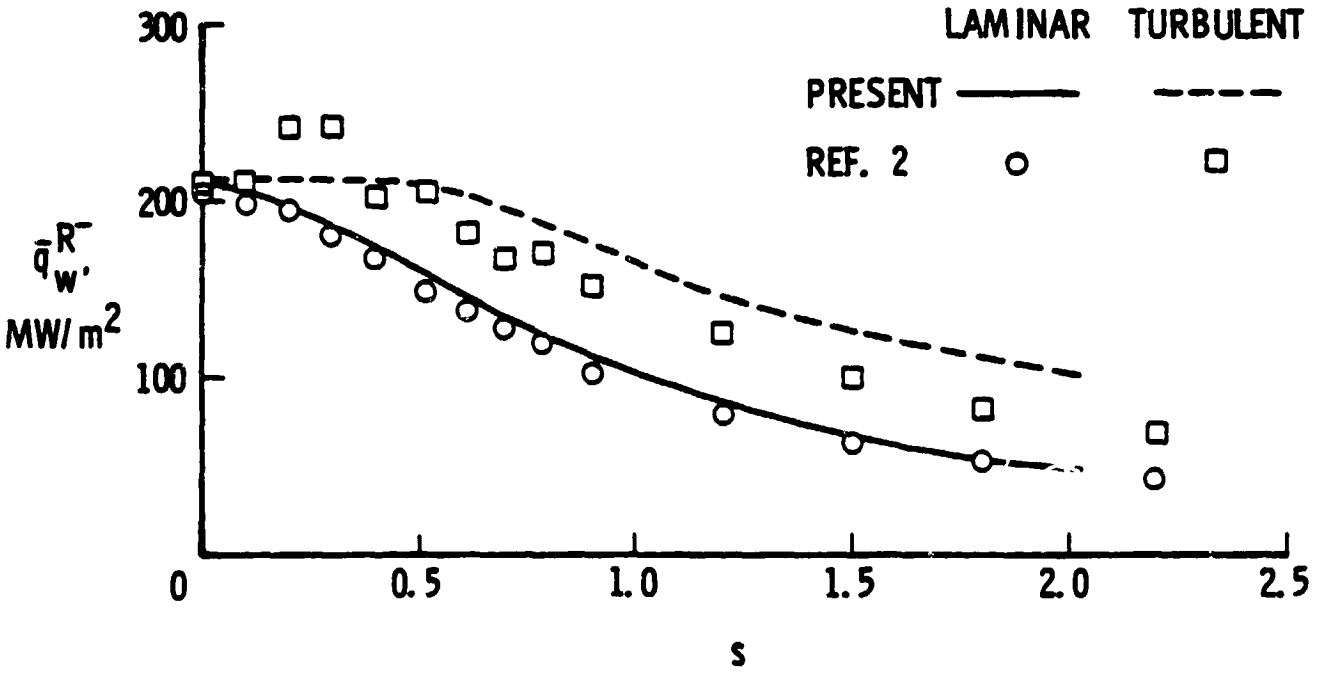

Figure 4. Comparison of coupled radiative heating rates for a 35-degree hyperboloid at 111.3 sec.

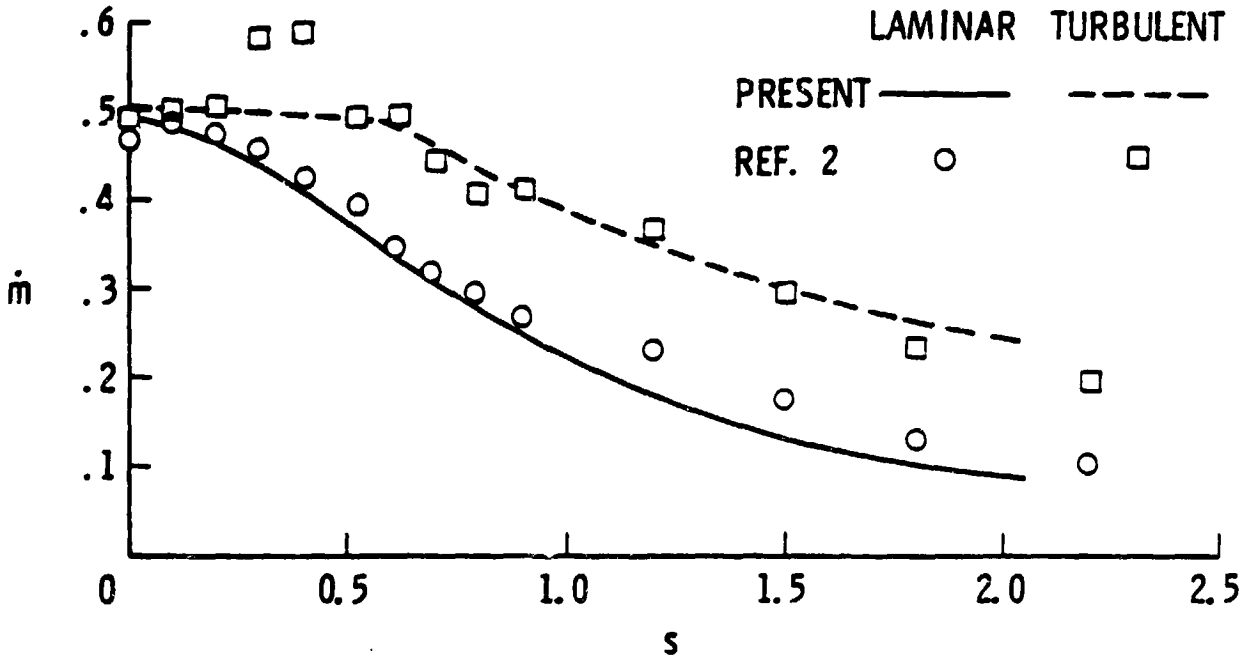

Figure 5. Comparison of coupled carbon-phenolic mass injection rates for a 35-degree hyperboloid at 111.3 sec.

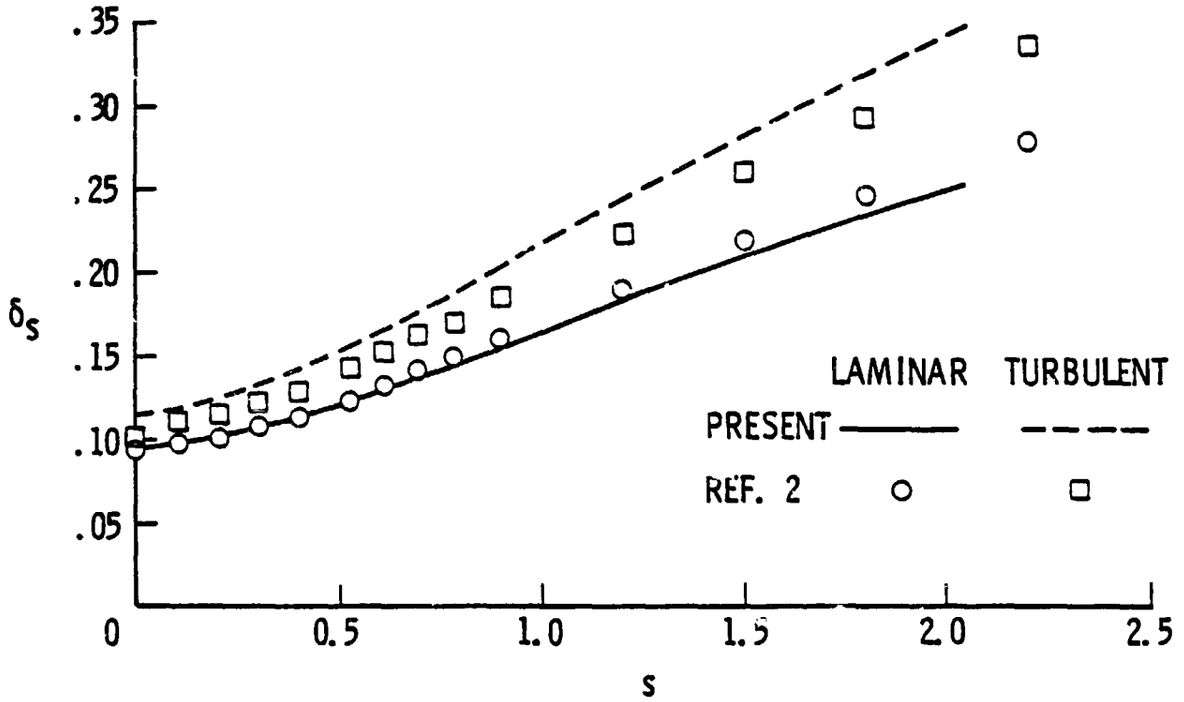

Figure 6. Comparison of shock shapes for a 35-degree hyperboloid at 111.3 sec.

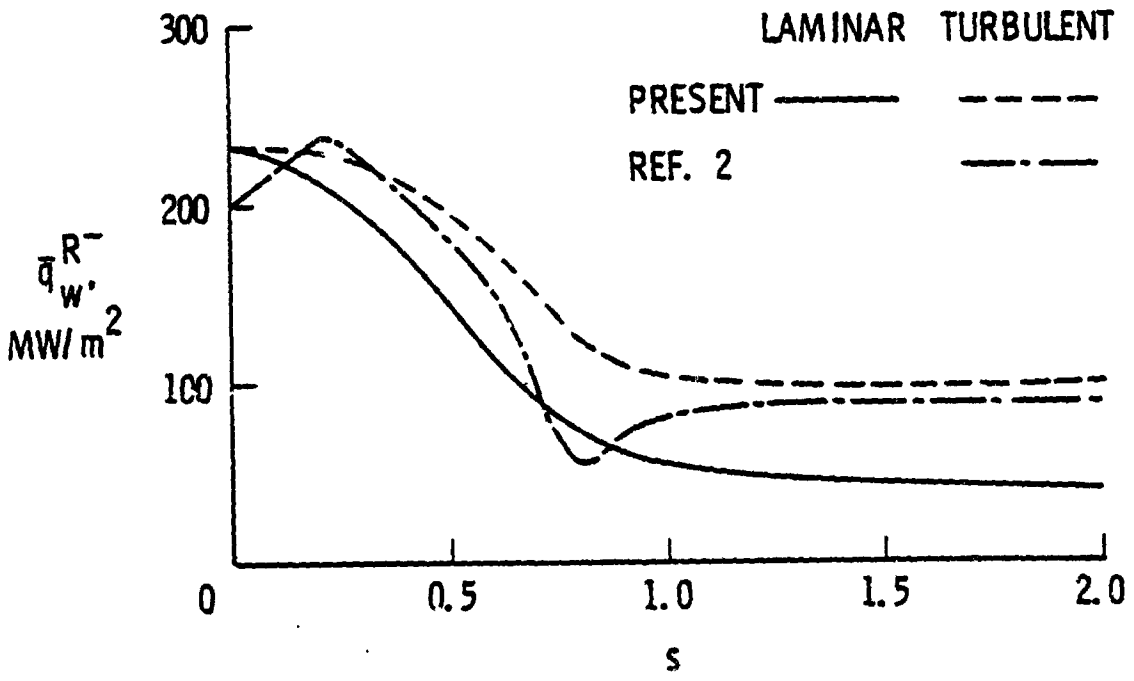

Figure 7. Comparison of coupled radiative heating rates for a 45-degree sphere cone at 111.3 sec.

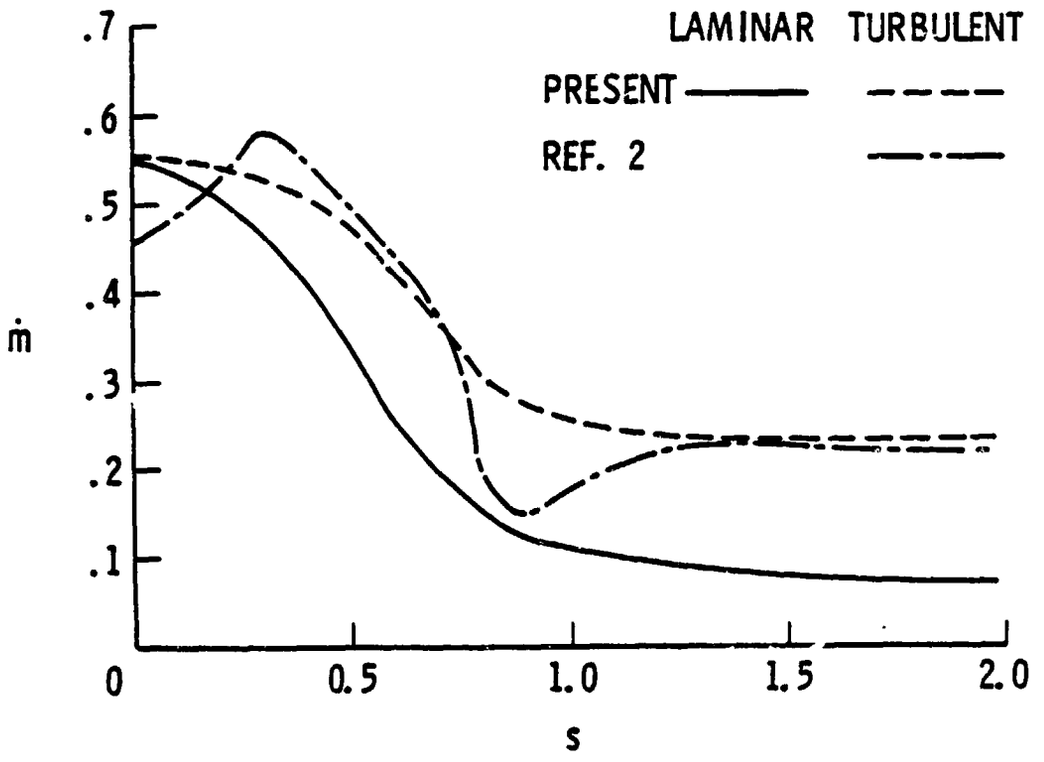

Figure 8. Comparison of coupled carbon-phenolic mass injection rates for a 45-degree sphere cone at 111.3 sec.

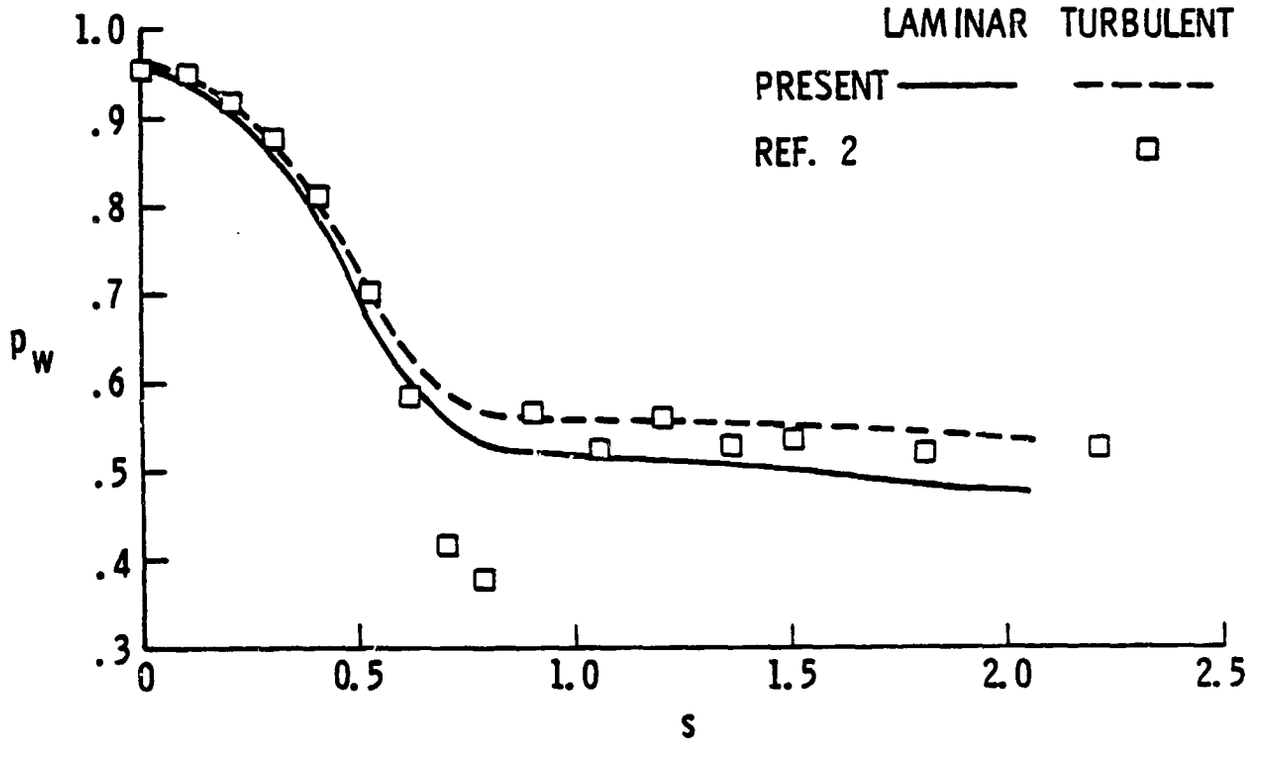

Figure 9. Comparison of surface pressure distribution for a 45-degree sphere cone at 111.3 sec.

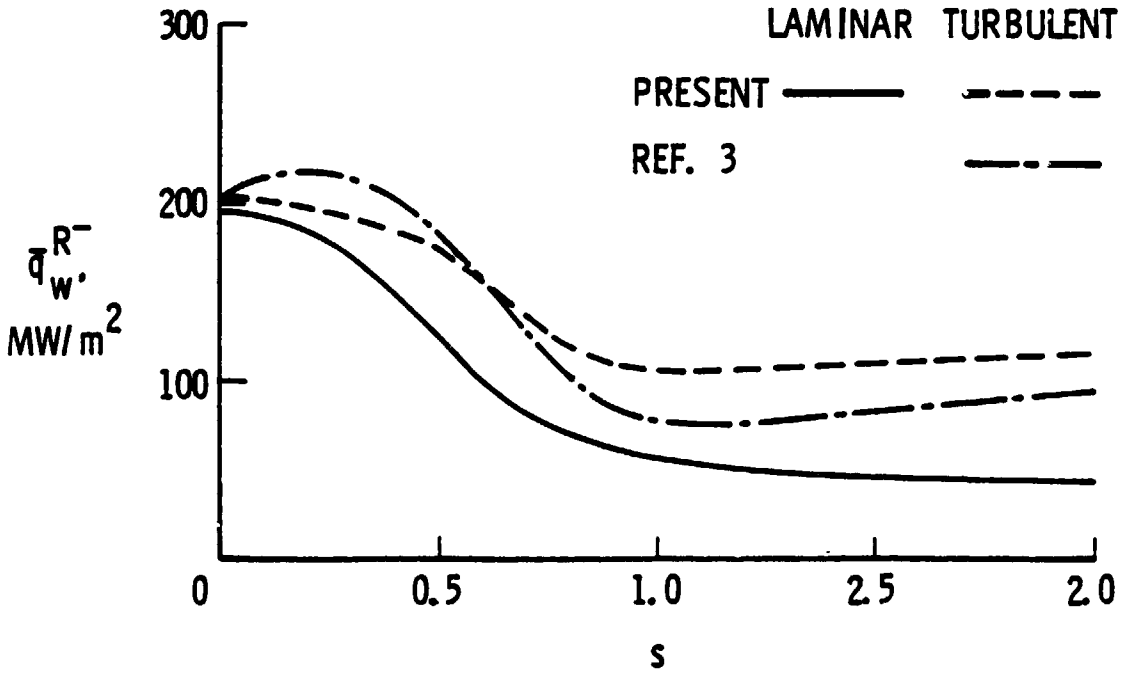

Figure 10. Comparison of coupled radiative heating rates for a 45-degree sphere cone at 109 sec.

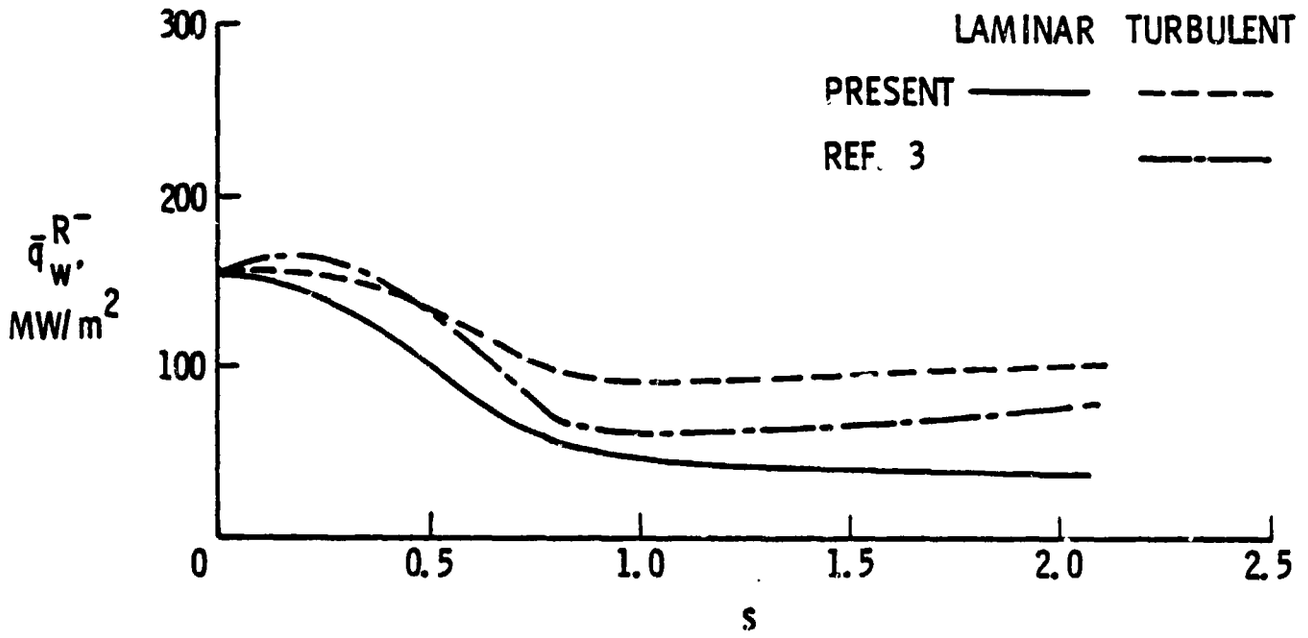

Figure 11. Comparison of coupled radiative heating rates for a 45-degree sphere cone at 107.2 sec.

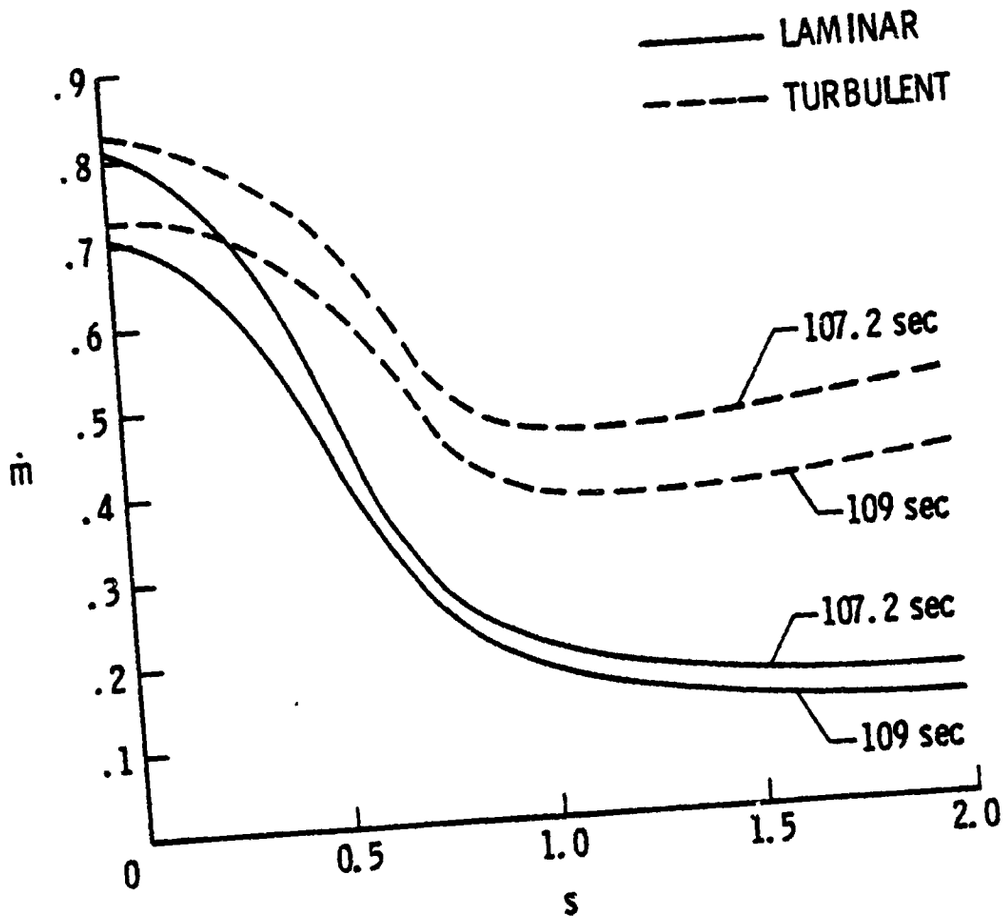

Figure 12. Coupled carbon-phenolic mass injection rates for a 45-degree sphere cone.

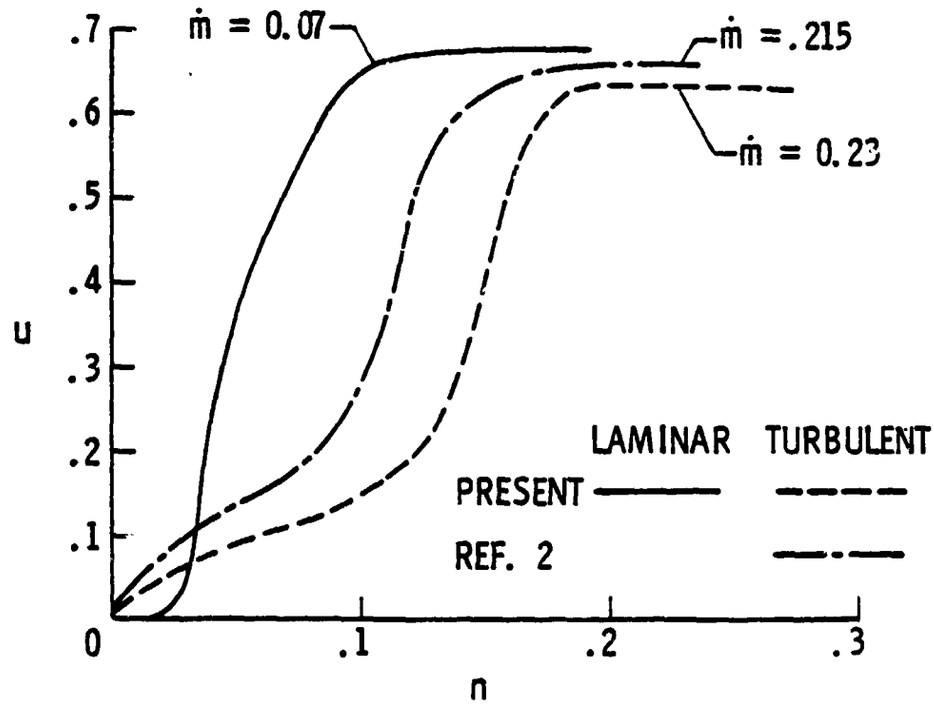

Figure 13. Comparison of turbulent tangential velocity profiles at s = 1.8 for a 45-degree sphere cone at 111.3 sec.

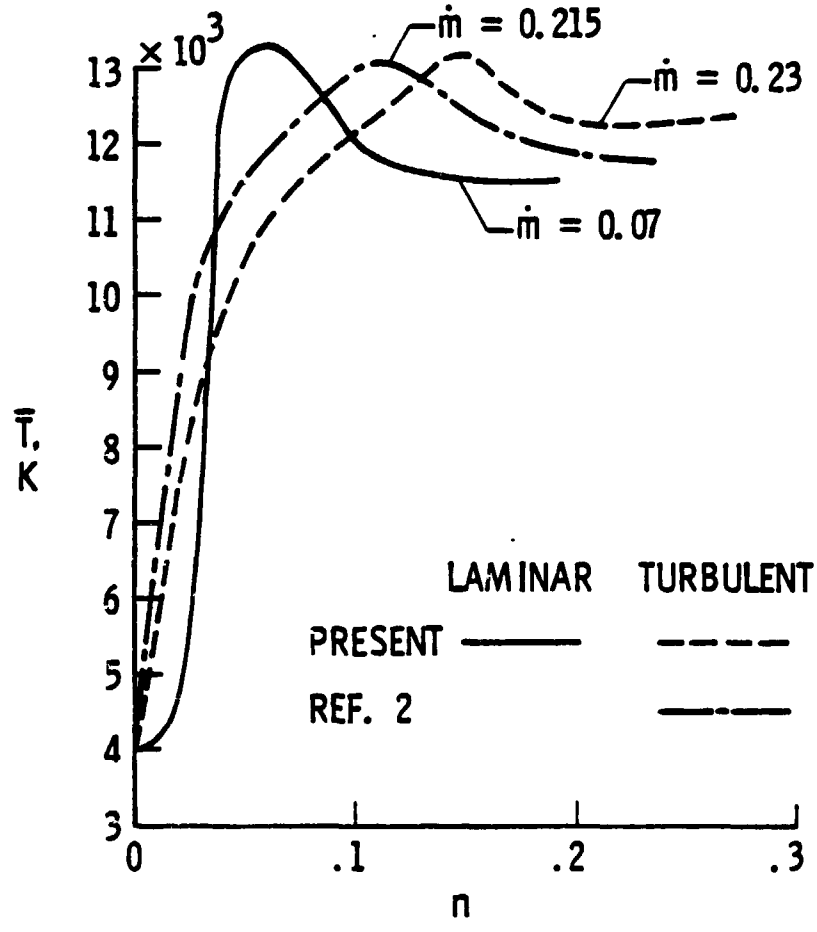

Figure 14. Comparison of turbulent temperature profiles at s = 1.8 for a 45-degree sphere cone at 111.3 sec.

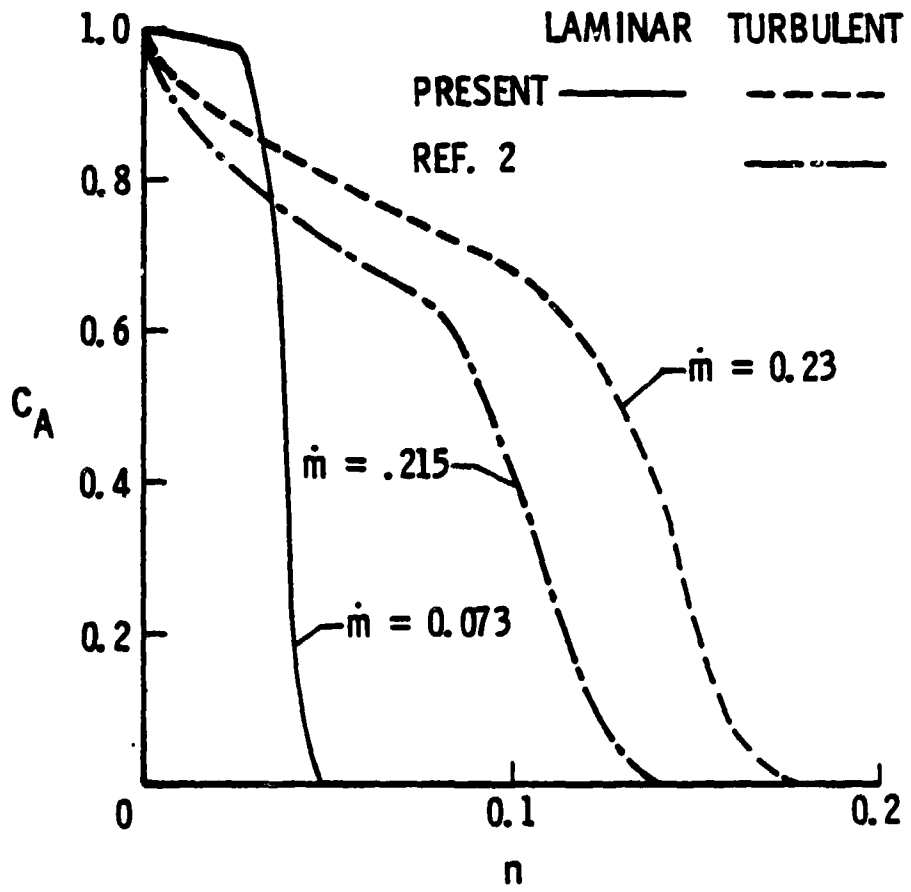

Figure 15. Effect of turbulence on ablation mass fraction profile at s = 1.8 for a 45-degree sphere cone at 111.3 sec.

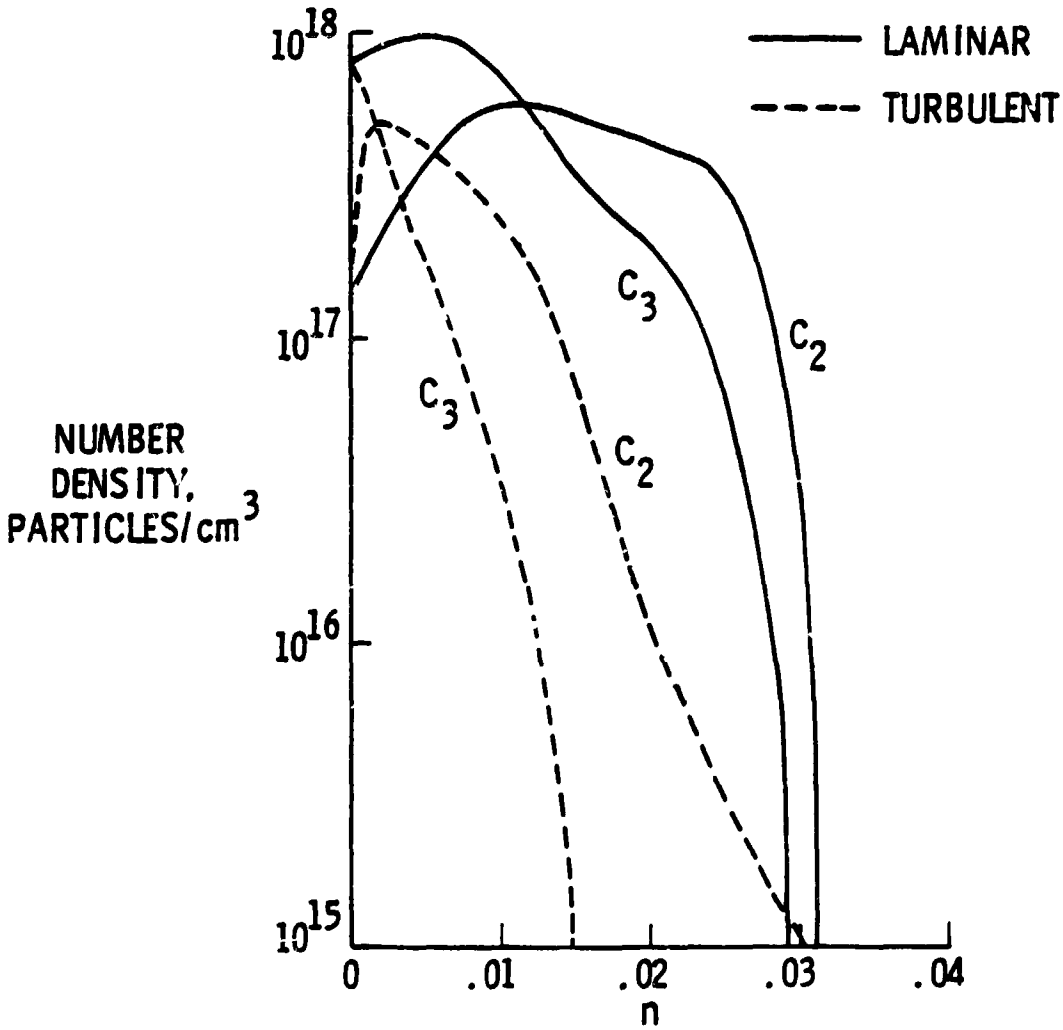

Figure 16. Effect of turbulence on concentrations of major radiation absorbers at s = 1.8 for a 45-degree sphere cone at 111.3 sec.

REFERENCES

1. Moss, J. N., Anderson, E. C., and Simmonds, A. L.: The Impact of Turbulence on a Radiating Shock Layer With Coupled Ablation Injection. AIAA Paper No. 78-1186, July 1978.

2. Moss, J. N.: A Study of the Aerothermal Entry Environment for the Galileo Probe. AIAA Paper No. 79-1081, June 1979.

3. Nicolet, W. E.; and Balakrishnan, A.: Methods for Predicting Off-Stagnation Point Flow-Fields for Planetary Entry Probes. AIAA Paper No. 79-1083, June 1979.

4. Kumar, A.; and Graves, R. A., Jr.: Numerical Solution of the Viscous Hypersonic Flow past Blunted Cones at Angle of Attack. AIAA Paper No. 77-172, Jan. 1977; also AIAA, Vol. 15, Aug. 1977, pp. 1061-1062.

5. Kumar, A.; Tiwari, S. N.; and Graves, R. A., Jr.: Effects of Small Angle of Attack on the Radiating Viscous Shock Layer Solutions for Jovian Entry. AIAA Paper No. 78-909, May 1978; also AIAA Progress in Astronautics and Aeronautics - Outer Planet Entry Heating and Thermal Protection, Vol. 64, edited by R. Viskanta, N. Y., 1979, pp. 147-164.

6. Kumar, A.; Graves, R. A., Jr.; and Tiwari, S. N.: Laminar and Turbulent Flows Over a Spherically Blunted Cone With Massive Surface Blowing. AIAA, Dec. 1979.

7. Nicolet, W. E.: Advanced Methods for Calculating Radiation Transport in Ablation-Product Contaminated Boundary Layers. NASA CR 1656, 1970.

8. Nicolet, W. E.: User's Manual for the Generalized Radiation Transfer Code (RAD/EQUIL). NASA CR-116353, 1969.

9. Sutton, K.; and Moss, J. N.: Radiation Absorption by the C_2 Band Systems for Jupiter Entry Conditions. AIAA Paper No. 79-0033, Jan. 1979.

10. Moss, J. N.; Jones, J. J.; and Simmonds, A. L.: Radiative Flux Penetration Through a Blown Shock Layer for Jupiter Entry. AIAA Paper No. 78-908. May 1978; also AIAA Progress in Astronautics and Aeronautics - Outer Plant Entry Heating and Thermal Protection, Vol. 64, edited by R. Viskanta, N. Y., 1979, pp. 22-41.

11. Stroud, C. W.; and Brikley, K. L.: Chemical Equilibrium of Ablation Materials Including Condensed Species. NASA TN D-5391, 1969.

12. Kumar, A.; Graves, R. A., Jr.; and Weilmuenster, K. J.: User's Guide for the Vectorized Code "EQUIL" for Calculating Equilibrium Chemistry on CDC-STAR-100 Computer. NASA TM 80193, 1980.

13. Wilke, C. R.: A Viscosity Equation for Gas Mixtures. J. Chem. Phys., Vol. 18, No. 4, Apr. 1950, pp. 517-519.

14. Clauser, F. H. The Turbulent Boundary Layer, Vol. IV of Advances in Applied Mathematics. H. L. Dryden and Th. Von Kármán, eds., Academic Press, Inc., 1956, pp. 1-51.

15. Klebanoff, P. S.: Characteristics of Turbulence in a Boundary Layer With Zero Pressure Gradient. NACA Report 1247, 1955.

16. Cebeci, T.: Behavior of Turbulent Flow Near a Porous Wall With Pressure Gradient. AIAA, Vol. 8, No. 12, Dec. 1970, pp. 2152-2156.

17. Anderson, E. C.; and Wilcox, D. C.: Vorticity Interaction Effects on Blunt Bodies. NASA CR-2778, 1977.

18. MacCormack, R. W.: The Effect of Viscosity in Hypervelocity Impact Cratering. AIAA Paper No. 69-354, Apr. 1969.